Simulation of laser-induced incandescence measurements in an anisotropically scattering aerosol through backward Monte Carlo

Daun, K. J.; Thomson, Kevin; Liu, Fengshan

Publisher's version / Version de l'éditeur:
https://doi.org/10.1115/1.2955468
Journal of Heat Transfer, 130, November 11, pp. 112701-112710, 2008

Simulation of Laser-Induced Incandescence Measurements in an Anisotropically Scattering Aerosol Through Backward Monte Carlo

K. J. Daun[1]
e-mail: kjdaun@mme.uwaterloo.ca

K. A. Thomson

F. Liu

Institute for Chemical Process and Environmental Technology,
National Research Council of Canada,
1200 Montreal Road,
Ottawa, ON, K1A 0R6, Canada

Laser-induced incandescence (LII) measurements carried out in aerosols having a large particle volume fraction must be corrected to account for extinction between the energized aerosol particles and the detector, called signal trapping. While standard correction techniques have been developed for signal trapping by absorption, the effect of scattering on LII measurements requires further investigation, particularly the case of highly anisotropic scattering and along a path of relatively large optical thickness. This paper examines this phenomenon in an aerosol containing highly aggregated soot particles by simulating LII signals using a backward Monte Carlo analysis; these signals are then used to recover the soot particle temperature and soot volume fraction. The results show that inscattered radiation is a substantial component of the LII signal under high soot loading conditions, which can strongly influence properties derived from these measurements. Correction techniques based on Bouguer's law are shown to be effective in mitigating the effect of scatter on the LII signals. [DOI: 10.1115/1.2955468]

Introduction

Laser-induced incandescence (LII) is an established technique for measuring the properties of aerosols and is particularly well suited for characterizing soot within flames. In this procedure a nanosecond laser pulse energizes the particles contained within a small measurement volume to incandescent temperatures and the resulting radiance from these particles is measured using photodetectors, usually at several wavelengths in the near-infrared spectrum. The particle volume fraction within the measurement volume can then be inferred from the LII signal by comparing it to the signal obtained from an aerosol in which the particle volume fraction is known through an independent means, such as line-of-sight attenuation (LOSA) [1] or gravimetric sampling [2]. An alternative approach [3,4] is to first determine the particle temperature from the LII signals using multiwavelength pyrometry and then calculate the particle volume fraction by comparing the expected emission at that temperature to the observed incandescence signal. Because the particle cooling rate is inversely proportional to the specific surface area, the aerosol particle size distribution can also be found by deconvolving the time-resolved spectral incandescence intensity [5] or the pyrometrically defined temperature [6].

When the particle volume fraction is large, it is necessary to account for attenuation of the spectral incandescence due to extinction between the laser-energized aerosol particles and the detector; this effect is called *signal trapping* [7]. In combustion applications signal trapping is important in cases of high soot loading, such as flames in high ambient pressures [1] and buoyancy-driven turbulent flames [8], resulting in erroneous soot volume fraction measurements if the assumption of an optically thin medium does not hold [7]. Furthermore, since the extinction coefficients of soot-laden aerosols decrease with increasing wavelength, signal trapping causes pyrometrically defined temperatures to be underestimated [9,10], leading to errors in temperature, soot volume fraction, and temperature-based time-resolved LII particle sizing.

While it is becoming increasingly commonplace to correct the LII signal for trapping (e.g., Refs. [1,2,11–13]) most studies tacitly assume that the absorption coefficient is equal to the extinction coefficient, which in experiments involving soot-laden aerosols is usually justified by arguing that the primary particles act as independent Rayleigh scatters since their diameters almost always satisfy the required size parameter criterion [14]. While this treatment may be reasonable when the soot aggregates are very small, it is inappropriate for aerosols containing aggregates composed of large numbers of primary particles [15,16] typical in buoyant turbulent diffusion flames or carbon black reactors, for example. In these situations dependent scattering between primary particles is greatly enhanced and makes the scattering cross section of highly aggregated soot particles comparable in magnitude to the absorption cross section.

Accounting for signal trapping due to scattering is less straightforward than absorption alone, since the signal is simultaneously attenuated by outscattering and augmented by inscattered radiation along the path between the measurement volume and the detector; Murphy and Shaddix [17] and Liu et al. [9] show that, because of the highly forward scattering of soot aggregates, signal losses caused by outscatter are mitigated by inscatter. Due to the strong scattering of soot aggregates, Thomson et al. [18] raised the concern that in LII experiments in which a laser sheet is used instead of a beam inscattering of photons emitted from energized aerosol particles outside the detection volume could inflate the measured LII signal beyond the value one would expect without any scattering whatsoever. Nevertheless, to the best of the authors' knowledge no experimental LII study has yet to explicitly correct for the effect of in- and outscatter between the measurement volume and the detector.

[1]Corresponding author. Presently at Department of Mechanical and Mechatronics Engineering, University of Waterloo, 200 University Ave. W., Waterloo, ON, N2L 3G1, Canada.

Contributed by the Heat Transfer Division of ASME for publication in the JOURNAL OF HEAT TRANSFER. Manuscript received August 28, 2007; final manuscript received November 27, 2007; published online August 29, 2008. Review conducted by Walter W. Yuen. Paper presented at the 2007 ASME International Mechanical Engineering Congress (IMECE2007), Seattle, WA, November 10–16, 2007.

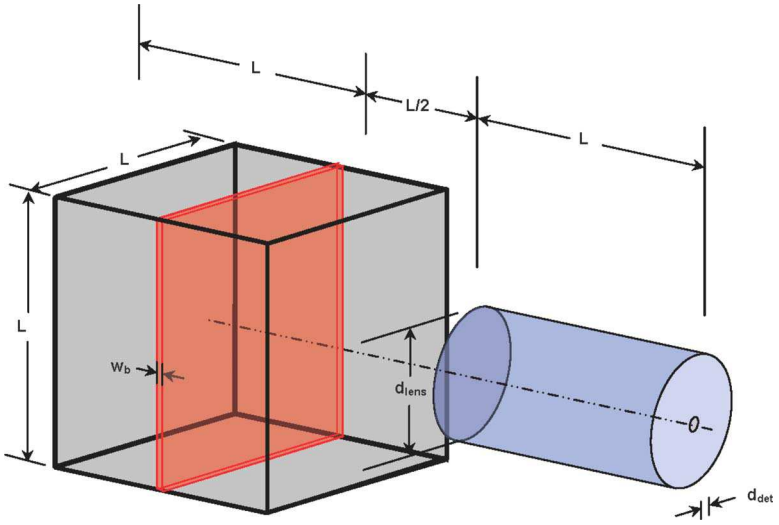

Fig. 1 Problem geometry for the sheet excitation case

This paper endeavors to elucidate the effect of in- and outscattering on LII measurement within aerosols containing highly aggregated soot particles, with a focus on the role inscattering plays when the aerosol particles are energized by a laser sheet instead of a beam. The analysis is done on a homogeneous aerosol containing soot aggregates typical of turbulent diffusion flames [8]. A backward Monte Carlo (BMC) analysis [19] is used to calculate the spectral incandescence measured by the simulated detector; this approach is well suited to this problem as it retains the accurate physics modeling associated with the standard Monte Carlo analysis but is far more efficient since only the photon bundles incident on the collection optics are traced to their emission locations. Although it has been used to simulate other types of optical measurement, to the authors' knowledge this is the first application of BMC to model LII.

The simulations show that outscattering is a major contributor to signal trapping, causing the pyrometric temperatures derived from LII signals to be underestimated, which in turn causes the soot volume fractions to be overestimated. This effect is less pronounced in the sheet excitation case since inscatter from aerosol particles within the sheet but outside the measurement volume offset signal losses due to trapping. We also evaluate several methods based on Bouguer's law [20], which are shown to be largely effective ways to account for signal trapping.

Problem Description

The analysis is carried out on a soot-laden aerosol at $T_g = 300$ K contained within a cubical enclosure having sides of length $L = 0.1$ m. The surroundings are also taken to be at 300 K. A spectral radiometer is located outside the enclosure and centered on the z-axis as shown in Fig. 1. Two excitation cases are considered: In the first case the aerosol particles are heated using a laser beam having a 2.5×2.5 mm^2 square profile, while in the second case a semi-infinite sheet having a 2.5 mm thickness is used to energize the particles. In both cases the particles within the beam reach a temperature, T_{beam}, of 3600 K. Figure 2 shows the details of the collection optics, consisting of a blackbody detector surface and a perfect lens. The detector surface has a diameter of 2.5 mm, while the lens has a diameter of 5 cm and a focal length of $L/2 = 5$ cm, which images the detector surface into the middle of the measurement volume. The intersection of the collection optics view angle and the laser beam or sheet carves out a roughly cylindrical measurement volume. The detection wavelengths are 400 nm and 780 nm, which are often used in real LII experiments.

The aerosol contains soot aggregates composed of various numbers of 30 nm diameter primary particles. The number of primary particles per aggregate obeys a log-normal distribution,

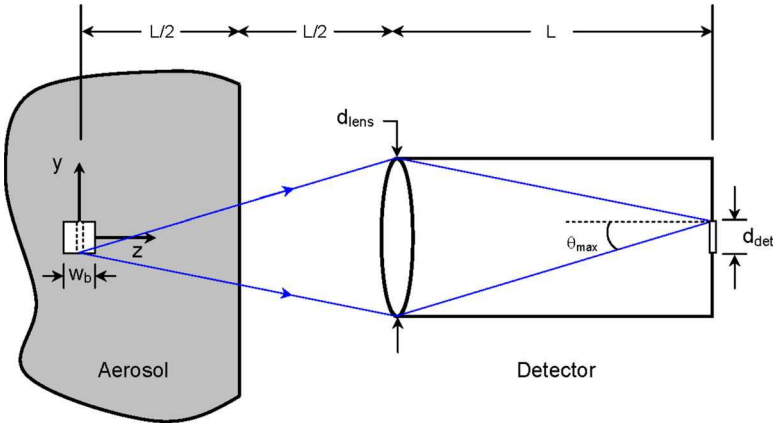

Fig. 2 Optics schematic shown for beam excitation case (not to scale)

$$P(N_p) = \frac{1}{N_p\sqrt{2\pi}\ln\sigma_g}\exp\left\{-\left[\frac{\ln(N_p/N_{p,g})}{\sqrt{2}\ln\sigma_g}\right]^2\right\} \quad (1)$$

where $N_{p,g}=200$ primary particles per aggregate and $\sigma_g=3$, parameters that are typical of soot in buoyant turbulent diffusion flames [8]. The aggregate structure is assumed to be mass fractal in nature, and the number of primary particles per aggregate is related to the radius of gyration, R_g, by [15,16]

$$N_p = k_g(2R_g/d_p)^{D_f} \quad (2)$$

where the fractal dimension and prefactor are set equal to $D_f=1.78$ and $k_g=2.3$, characteristic values for soot in flames [8]. The radius of gyration plays an important role in dependent scattering between the primary particles, which affects the aggregate scattering cross section and phase function as shown later.

The effects of scattering on the measured LII signal are evaluated at different soot loadings specified by the soot volume fraction, f_v, which is related to the aggregate number density, N_{agg}, by

$$N_{\text{agg}} = \frac{f_v}{\frac{\pi d_p^3}{6}\int_0^\infty N_p P(N_p)dN_p} = \frac{f_v}{\frac{\pi d_p^3}{6}\exp\{[N_{p,g}+(\ln\sigma_g)^2]/2\}} \quad (3)$$

Radiative Properties

Bulk radiative properties of the homogeneous medium are derived from the phase function and absorption and scattering cross sections of soot aggregates, which in turn are calculated using Rayleigh–Debye–Gans polyfractal aggregate (RDG-PFA) theory [8,15,16]. For independent primary particles, the absorption and scattering cross sections are obtained from Rayleigh theory [15,16]

$$C_a^p = \frac{4x_p^3 E(\mathbf{m})}{\pi\eta^2}, \quad C_s^p = \frac{8x_p^6 F(\mathbf{m})}{3\pi\eta^2} \quad (4)$$

where $E(\mathbf{m})=\text{Im}[(\mathbf{m}^2-1)/(\mathbf{m}^2+2)]$ is the complex absorption function, $F(\mathbf{m})=|[(\mathbf{m}^2-1)/(\mathbf{m}^2+2)]|$ is the complex scattering function, $\mathbf{m}=n+ik$ is the complex index of refraction of soot, $\eta=2\pi/\lambda$ is the wave number, and $x_p=\pi d_p/\lambda$ is the primary particle size parameter. The vertical and horizontal polarization cross sections of primary particles are given by

$$C_{vv}^p = \frac{x_p^6 F(\mathbf{m})}{\eta^2}, \quad C_{hh}^p = C_{vv}^p\cos^2\theta \quad (5)$$

where θ is the angle formed between the incident and the scattered radiation. (Both C_{hv}^p and C_{vh}^p are zero.)

Since primary particles are assumed to absorb and emit radiation independently, the absorption cross section of a soot aggregate containing N_p primary particles is simply

$$C_a^{\text{agg}} = N_p C_a^p \quad (6)$$

In contrast, since scattering by the primary particles within a soot aggregate is usually highly dependent, the aggregate scattering cross section can be much larger than the sum of primary particle scattering cross sections predicted by Rayleigh theory. The aggregate scattering cross section is given by [8]

$$C_s^{\text{agg}} = N_p^2 C_s^p g(\eta R_g, D_f) \quad (7)$$

where the aggregate total scattering factor, $g(\eta R_g, D_f)$, is equal to

$$g(\eta R_g, D_f) = 1 - 2(\eta R_g)^2/3, \quad (\eta R_g)^2 \le 3D_f/8 \quad (8)$$

in the Guinier regime and

Table 1 Radiative properties of the medium

	$\lambda=400$ nm	$\lambda=780$ nm
$\mathbf{m}$ [22]	$1.5+0.65i$	$1.63+0.49i$
$E(\mathbf{m})$	0.3170	0.2172
$F(\mathbf{m})$	0.4931	0.4546
$\bar{C}_a^{\text{agg}}$ ($\times 10^4$ nm^2)	7.67	4.31
$\bar{C}_s^{\text{agg}}$ ($\times 10^4$ nm^2)	2.70	0.69
$g_{\text{HG},\lambda}$	0.781	0.672

$$g(\eta R_g, D_f) = \frac{\beta}{2}(3-3\beta+2\beta^2) - \frac{(\eta R_g\beta)^2}{3}(3-4\beta+3\beta^2) + (2\eta R_g)^{-D_f}\left[\frac{3}{2-D_f} - \frac{12}{(6-D_f)(4-D_f)} - 3\beta^{1-D_f/2}\left(\frac{1}{2-D_f} - \frac{2\beta}{4-D_f} + \frac{2\beta^2}{6-D_f}\right)\right], \quad (\eta R_g)^2 > 3D_f/8 \quad (9)$$

in the power-law regime. The polarization cross section of the aggregate is

$$C_{vv}^{\text{agg}} = N_p^2 C_{vv}^p f(qR_g) = \frac{C_{hh}^{\text{agg}}}{\cos^2\theta} \quad (10)$$

where $q=2\eta\sin(\theta/2)$ is the modulus of the scattering vector and $f(q,R_g)$ is the form factor given by [21]

$$f(qR_g) = [1 + 8(qR_g)^2/(3D_f) + (qR_g)^8]^{-Df/8} \quad (11)$$

which applies over both the Guinier and power-law regimes.

Equations (4)–(11) provide the required equations to calculate the absorption, scattering, and polarization cross sections for a soot aggregate. When deriving the bulk radiative properties of the medium, however, it is necessary to account for the polydispersity of different-sized aggregates by calculating averaged cross sections using Eq. (1) [8],

$$\bar{C}_a^{\text{agg}} = \int_0^\infty C_a^{\text{agg}}(N_p)P(N_p)dN_p \quad (12)$$

with similar expressions for $\bar{C}_s^{\text{agg}}$ and $\bar{C}_{vv}^{\text{agg}}$, and again, $\bar{C}_{hh}^{\text{agg}} = \bar{C}_{vv}^{\text{agg}}/\cos^2\theta$. The absorption and scattering coefficients are then $\alpha_\lambda = N_{\text{agg}}\bar{C}_a^{\text{agg}}$ and $\sigma_{s\lambda} = N_{\text{agg}}\bar{C}_s^{\text{agg}}$, respectively, while the scattering phase function is given by

$$\Phi(\theta) = \frac{4\pi}{\bar{C}_s^{\text{agg}}}\frac{(\bar{C}_{vv}^{\text{agg}} + \bar{C}_{hh}^{\text{agg}})}{2} \quad (13)$$

Following the above calculations for soot aggregates at the detection wavelengths of 400 nm and 780 nm and assuming $\mathbf{m}=1.5+0.65i$ at $\lambda=400$ nm and $\mathbf{m}=1.63+0.49i$ at $\lambda=780$ nm [22] results in the average absorption and scattering cross sections in Table 1, and the phase functions shown in Fig. 3 evaluated at 181 angles evenly spaced between $0\le\theta\le\pi$. These values are closely interpolated by Heyney–Greenstein phase functions having the form

$$\Phi(\theta) = \frac{1-g_{\text{HG}\,\lambda}^2}{(1+g_{\text{HG}\,\lambda}^2 - 2g_{\text{HG},\lambda}\cos\theta)^{3/2}} \quad (14)$$

where the anisotropy factors, $g_{\text{HG},\lambda}$, determined by least-squares fitting are also included in Table 1.

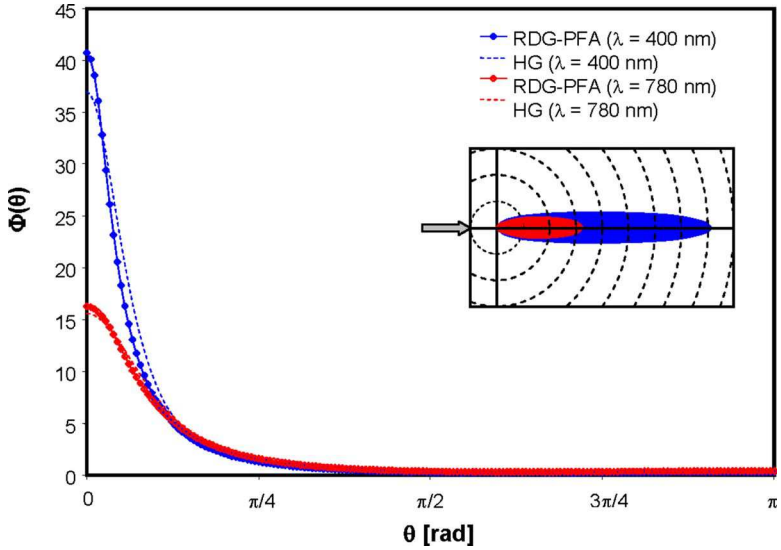

Fig. 3 Scattering phase functions

Radiation Analysis Through Backward Monte Carlo

The objective of this analysis is to evaluate how scattering affects LII measurements and soot volume fractions and pyrometric temperatures derived from these measurements, which requires calculation of the spectral radiant energy incident on the detector surface at the detection wavelengths. The radiation field is governed by the radiative transfer equation (RTE)

$$\mathbf{s}\cdot\nabla I_\lambda(\mathbf{r},\mathbf{s}) = -\kappa_\lambda I_\lambda(\mathbf{r},\mathbf{s}) + \alpha_\lambda I_{b\lambda}(\mathbf{r}) + \frac{\sigma_{s\lambda}}{4\pi}\int_0^{4\pi} I_\lambda(\mathbf{r},\mathbf{s}')\Phi_\lambda(\mathbf{s}',\mathbf{s})d\Omega \tag{15}$$

subject to

$$I_\lambda(\mathbf{r}_w,\mathbf{s}) = I_{\lambda w}(\mathbf{r}_w,\mathbf{s}) \tag{16}$$

where s is a unit vector, $\mathbf{r}$ is the position vector from the origin, $\mathbf{r}_w$ denotes a location on the boundary, $\kappa_\lambda = \alpha_\lambda + \sigma_{s\lambda}$, and $I_{b,\lambda}(\mathbf{r})$ is the blackbody intensity at $\mathbf{r}$ and λ. (Note that the radiative properties are homogeneous over the problem domain and are thus independent of $\mathbf{r}$.) The analysis is considerably simplified by neglecting the contributions of blackbody emission from the surroundings and the medium at 300 K at the detection wavelengths, which are small relative to the spectral blackbody intensity of the energized particles at 3600 K.

Despite this simplification solving the radiative transfer equation over the entire problem domain remains computationally expensive, particularly if the solution is carried out using a standard, or forward, Monte Carlo-type analysis. In its traditional implementation, photon bundles are emitted at various locations throughout the medium and ray traced to their termination. Since a very small fraction of these bundles would terminate on the detector surface, a large number of bundles would need to be emitted and ray traced to achieve an acceptable level of variance in the solution.

A more efficient approach is the BMC method presented by Modest [19] based on the reciprocity relation for the RTE derived by Case [23]. In this implementation, which uses pathlength-based energy partitioning [19,24], a bundle (say, the nth bundle) is ray traced backward from an absorption location on the detector surface given by

$$\mathbf{C}_0^n = r^n\cos\psi^n\hat{\mathbf{i}} + r^n\sin\psi^n\hat{\mathbf{j}} - 2L\hat{\mathbf{k}} \tag{17}$$

and in a direction

$$\mathbf{i}_0^n = \cos\phi^n\sin\theta^n\hat{\mathbf{i}} + \sin\phi^n\sin\theta^n\hat{\mathbf{j}} - \cos\theta^n\hat{\mathbf{k}} \tag{18}$$

The random deviates in Eqs. (17) and (18) are sampled from expressions derived from probability density functions,

$$r^n = \frac{d_{\text{det}}}{2}\sqrt{R_r^n}, \quad \psi^n = 2\pi R_\psi^n \tag{19}$$

and

$$\sin\theta^n = \sqrt{R_\theta^n}\sin\theta_{\max}, \quad \phi^n = 2\pi R_\phi^n \tag{20}$$

where R_r^n, R_ψ^n, R_θ^n, and R_ϕ^n are random uniform deviates. In Eq. (20) $\theta_{\max}$ is the maximum detector acceptance angle; although the detector surface acts as a blackbody, Fig. 2 shows that any ray passing from the aerosol through the lens can only reach the detector surface if $\theta^n < \tan^{-1}[(d_{\text{det}}+d_{\text{lens}})/2L]$, so $\theta_{\max}$ is set equal to this value to improve the efficiency of the simulation.

The nth bundle is then ray traced backward to its emission location through a series of random scattering events, the distance between scattering events being sampled from

$$l_s^{n,j} = \frac{1}{\sigma_{s\lambda}}\ln\frac{1}{R_\sigma^{n,j}} \tag{21}$$

starting at $j=0$. At each scattering event, a new scattering distance is sampled from Eq. (21) and a new random direction specified by polar and azimuthal angles, $\theta^{n,j}$ and $\phi^{n,j}$, measured relative to the prescattered direction is sampled according to

$$R_\theta^{n,j} = \int_o^{\theta^{n,j}}\Phi(\theta^*)\sin(\theta^*)d\theta^* \tag{22}$$

and $\phi^{n,j} = 2\pi R_\phi^{n,j}$. In the case of a Heyney–Greenstein phase function, Eq. (22) is equivalent to [25]

$$\cos\theta^{n,j} = \frac{1}{2g_{\text{HG},\lambda}}\left[1 + g_{\text{HG},\lambda}^2 - \left(\frac{1-g_{\text{HG},\lambda}^2}{1+g_{\text{HG},\lambda}-2g_{\text{HG},\lambda}R_\theta^{n,j}}\right)\right] \tag{23}$$

This process continues until the bundle reaches the boundary, at which point ray tracing terminates. Following this procedure results in a piecewise-straight bundle path l^n extending backward from the detector to the boundary, as shown in Fig. 4.

The intensity incident on the detector surface due to the nth bundle is then found by integrating the intensity forward along l^n

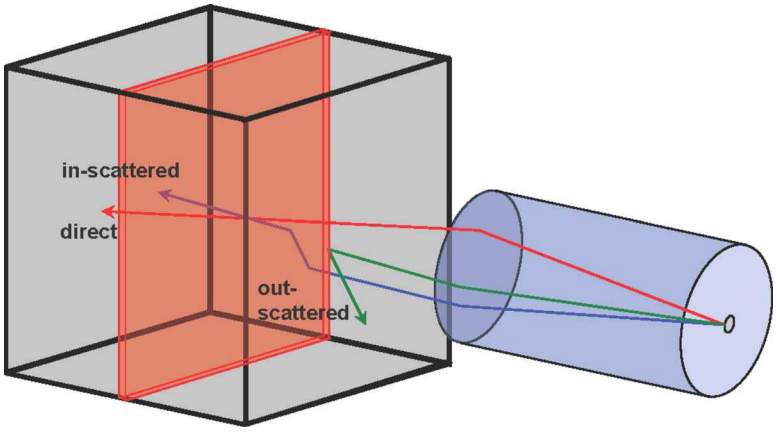

Fig. 4 Bundles emitted backward from the detector surface either travel directly to the beam are inscattered to the beam or outscattered away from the beam

from the domain boundary to the detector surface. Since the boundary is cold and black, this path integration simplifies to

$$I_\lambda^n = \int_0^{l^n} \alpha_\lambda I_{b\lambda}(\mathbf{r}')\exp[-\alpha_\lambda l'(\mathbf{r}')]dl' \tag{24}$$

(Note that the intensity along a ray traced through the perfect lens is conserved; a detailed proof is provided in Ref. [26].) Equation (24) is further simplified by splitting the path integral into two sets of m segments, the first containing m' segments that lie within the beam while the second set contains the remaining $m-m'$ segments that lie outside the beam. This latter set can be excluded from the integration since $I_{b\lambda}$ is negligible outside the beam, resulting in

$$l_\lambda^n = I_{b\lambda}(T_{\text{beam}})\sum_{j=1}^{m'} [\exp(-\alpha_\lambda l_{j,\text{in}}^n) - \exp(-\alpha_\lambda l_{j,\text{out}}^n)] \tag{25}$$

where $l^n{}_{j,\text{in}}$ and $l^n{}_{j,\text{out}}$ denote the distances along l^n from the detector surface to the location, where the jth segment enters and leaves the beam, respectively.

Finally, the spectral radiant heat absorbed by the detector is found by integrating the intensity from a large number of trial bundles

$$q_{\text{det},\lambda} = \int_0^{d_{\text{det}}/2}\int_0^{2\pi}\int_0^{\theta\,\max} I_{\lambda,\text{in}}(\theta,\phi)2\pi r\cos\theta\sin\theta d\theta d\phi dr$$

$$\approx \frac{\pi^2\sin^2\theta_{\max}d_{\text{det}}^2}{4N}\sum_{n=1}^{N} I_\lambda^n \tag{26}$$

Results and Discussion

The BMC simulation is performed on the problem at soot volume fractions over the range $10^{-8} \leqslant f_v \leqslant 10^{-5}$. (At this level of soot loading the aggregates are spaced sufficiently far apart so as to scatter independently [13].) When calculating $q_{\text{det},\lambda}$, bundles are continually ray traced from the detector surface in subsets of 100; and ray traced in subsets of 100; the total number of bundles is progressively doubled until the standard deviation of the mean in the spectral radiant energy absorbed by the detector, Eq. (26), is less than 1% of the average value. Each bundle emission has one of three outcomes corresponding to direct (unscattered) radiation, inscattered radiation, and outscattered radiation, as shown in Fig. 4: The bundle may travel directly from the detector to the measurement volume without undergoing a scattering event, be scattered from its original direction but still pass through the energized particles at some point along its path, or be scattered and intercept the domain boundary without passing through the energized zone.

The suitability of BMC to this application is first demonstrated by comparing the number of bundles that need to be emitted by the BMC technique to estimate the detector signal at 400 nm for the case of beam excitation at different soot volume fractions, compared to the number required by a forward, pathlength-based technique [24]. (The computational effort required to trace a ray path is similar for both techniques.) Figure 5 shows that the required number of bundles generally increases with soot loading in the BMC case since fewer of the bundles traced from the detector pass through the beam as f_v becomes large due to outscattering. Nevertheless, BMC requires far fewer bundles than the forward Monte Carlo (FMC) technique to obtain the same level of solution accuracy, and is consequently better suited to this problem.

Figure 6 shows the spectral radiant flux incident on the detector at 400 nm and 780 nm as a function of soot volume fraction. The straight lines on the log-log charts correspond to cases where extinction between the measurement volume and the detector surface is neglected and only direct emission from the energized particles is considered, in which case the spectral intensity incident on the detector due to measurement volume incandescence is

$$I_{\text{det},\lambda} \approx I_{b,\lambda}(T_{\text{beam}})[1-\exp(-w_b\alpha_\lambda)] \tag{27}$$

where w_b is the beam width. The detector incandescence is thus an exponential function of α_λ, which is directly proportional to f_v as expected from Eqs. (3) and (6). The actual detector signals initially follow the emission-only cases at low soot loadings but depart these trends as f_v becomes larger and signal trapping becomes more important. The signals at 400 nm depart from the emission-only line at lower values of f_v compared to the 780 nm signal because the extinction coefficients are larger at shorter wavelengths. The LII signals from sheet excitation are somewhat larger than those obtained using beam excitation due to inscatter from the energized particles located within the laser sheet but outside the measurement volume.

To further demonstrate the effect of inscatter on signal strength, the ratio of detector signal due to direct, nonscattered radiation to the total detector signal is plotted as a function of soot volume fraction in Fig. 7. At low soot loading the ratio is close to unity, indicating that the signal is almost entirely due to direct emission from the measurement volume. At higher soot loadings, however, inscatter makes up a larger portion of the signal. This effect is more pronounced at 400 nm than at 780 nm, and for sheet excitation compared to beam excitation for the reasons described above.

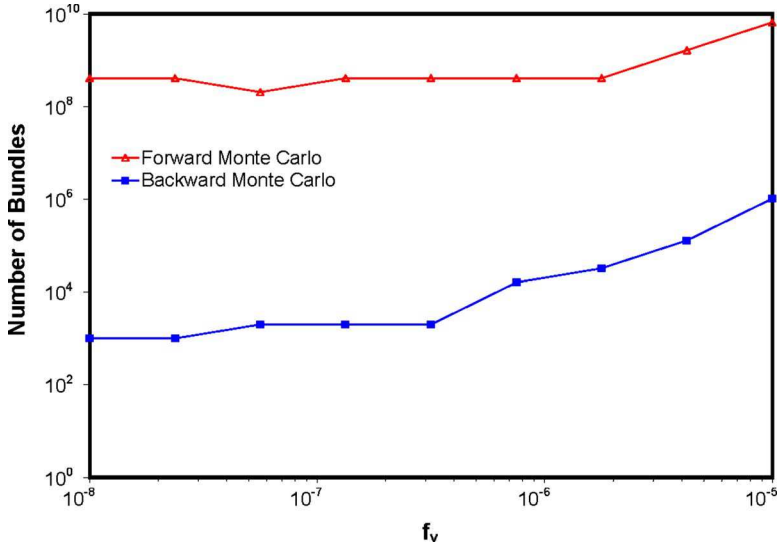

Fig. 5 Comparison of FMC and BMC efficiencies for the beam excitation case at λ_d=400 nm

We next investigate several corrections for signal trapping based on Bouguer's law [20] that have the form

$$q_{\mathrm{det},\lambda}^{\mathrm{corr}} = \frac{q_{\mathrm{det},\lambda}}{\exp(-\kappa_{\lambda,\mathrm{eff}} L/2)} \tag{28}$$

where $L/2$ is the distance between the measurement volume and the aerosol boundary as shown in Fig. 2 and $\kappa_{\lambda,\mathrm{eff}}$ is an effective spectral extinction coefficient. In many LII studies the scattering cross section is assumed to be negligible compared to the absorption cross section because the primary particle diameters satisfy the size parameter criterion for Rayleigh scattering. (While this is reasonable in some experiments, it is certainly erroneous for aerosols containing highly aggregated soot particles.) In these situations the extinction coefficient is set equal to the absorption coefficient, i.e., $\kappa_{\lambda,\mathrm{eff}}=\alpha_\lambda$, which in turn can be estimated using

$$\alpha_\lambda = \frac{6\pi E(\mathbf{m}_\lambda) f_v}{\lambda} \tag{29}$$

if the soot volume fraction is known a priori (e.g., Ref. [2]). In other cases, the extinction coefficient is inferred through supplemental LOSA experiments (e.g., Refs. [1,7,11–13]); in most LOSA experiments the optics are designed to exclude inscatter so the extinction coefficient likely to be measured approaches $\kappa_{\lambda,\mathrm{eff}} = \alpha_\lambda + \sigma_{s\lambda}$, even in aerosols that contain strongly forward scattering particles. As a final alternative, Liu et al. [9] adopt a modified extinction coefficient originally developed by Liu et al. [27] that accounts for inscatter using the Heyney–Greenstein anisotropy factor,

$$\kappa_{\lambda,\mathrm{eff}} = \alpha_\lambda + (1 - g_{\mathrm{HG},\lambda})\sigma_{s\lambda} \tag{30}$$

Figures 8 and 9 show detector signals obtained using the correction schemes, the uncorrected signal, and the emission-only case for beam and sheet excitations at 400 nm. (Signals at 780 nm follow the same trends but deviate less from the emission-only case since scattering is less pronounced at longer wavelengths.) Although setting $\kappa_{\lambda,\mathrm{eff}}=\alpha_\lambda$ is an improvement over the uncorrected signal it does not completely offset signal losses due to outscattering, particularly for the case of beam excitation. On the other hand, setting $\kappa_{\lambda,\mathrm{eff}}=\alpha_\lambda+\sigma_{s\lambda}$ overestimates the LII signals since this correction neglects inscattering contributions; this effect

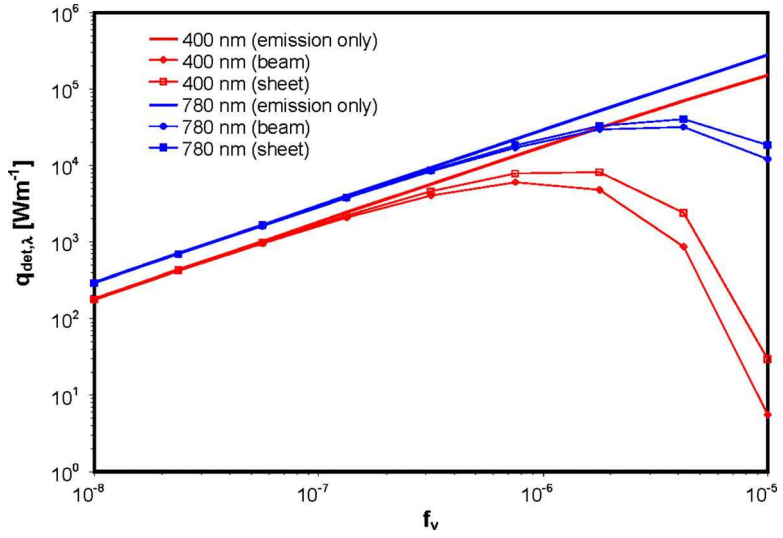

Fig. 6 Detector signal versus soot volume fraction

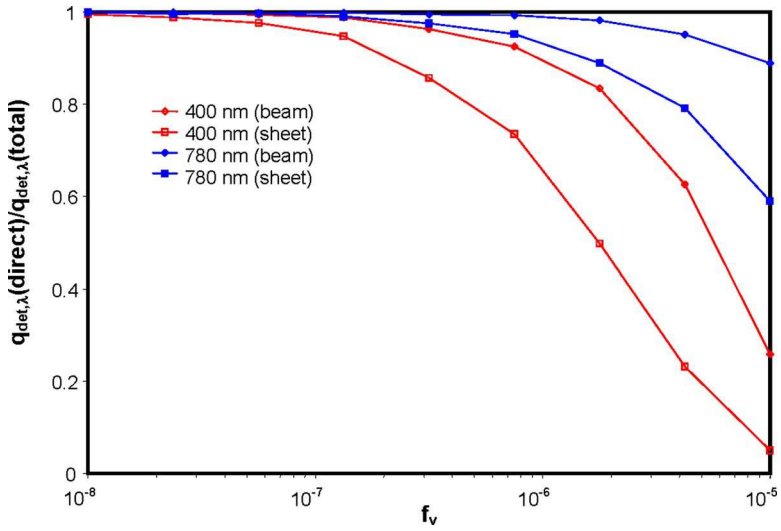

Fig. 7 Ratio of direct to total detector flux versus soot volume fraction

is most pronounced for sheet excitation at λ_d=400 nm. The best correction scheme is Eq. (30), although this technique also fails in the 400 nm beam excitation case at high soot loading. Furthermore, the anisotropy factor can only be determined if the scattering phase function is available, either by independent experimental measurement or if the soot morphology distribution parameters are known with certainty.

LII signals are often used to infer a pyrometric temperature and soot volume fraction. The impact of signal trapping on these measurements and the effectiveness of the correction schemes are assessed by calculating these parameters using the signals shown in Figs. 8 and 9. By invoking Wein's assumption, i.e., that $\exp(hc_0/\lambda k_B T_{\text{beam},m})$ is much larger than unity, the pyrometric beam temperature is found from Ref. [28]

$$T^w_{\text{beam},m} = \frac{\dfrac{hc_0}{k_B}\left(\dfrac{1}{\lambda_2}-\dfrac{1}{\lambda_1}\right)}{\ln\left[\dfrac{q_{\text{det},\lambda 1}}{q_{\text{det},\lambda 2}}\left(\dfrac{\lambda_1}{\lambda_2}\right)^6 \dfrac{E(\mathbf{m}_{\lambda 1})}{E(\mathbf{m}_{\lambda 2})}\right]} \tag{31}$$

where h is Planck's constant, k_B is Boltzmann's constant, and c_0 is the speed of light. The error induced by Wein's approximation is then corrected using the iterative procedure of Levendis et al. [29],

$$T_{\text{beam},m} = \frac{\dfrac{hc_0}{k_B}\left(\dfrac{1}{\lambda_2}-\dfrac{1}{\lambda_1}\right)}{\ln\left[\dfrac{q_{\text{det},\lambda 1}}{q_{\text{det},\lambda 2}}\left(\dfrac{\lambda_1}{\lambda_2}\right)^6 \dfrac{1-\exp(-hc_0/\lambda_1 k_b T^w_{\text{beam},m})}{1-\exp(-hc_0/\lambda_2 k_b T^w_{\text{beam},m})}\right]} \tag{32}$$

which usually provides a satisfactory result in a single iteration. Once the pyrometric temperature is known, the soot volume fraction can be calculated using the autocorrelated method of Snelling et al. [28],

$$f_{v,m} = \frac{q_{\text{det},\lambda}}{\Phi_p(T_{\text{beam},m},\lambda) M^2 A_{\text{detector}} A_{\text{lens}} w_b} 4\pi L^2 \tag{33}$$

where M is the magnification (equal to unity), A_{detector} and A_{lens} are the surface areas of the detector and lens, and Φ_p is the total radiated power per unit volume of particulate at detection wavelength λ,

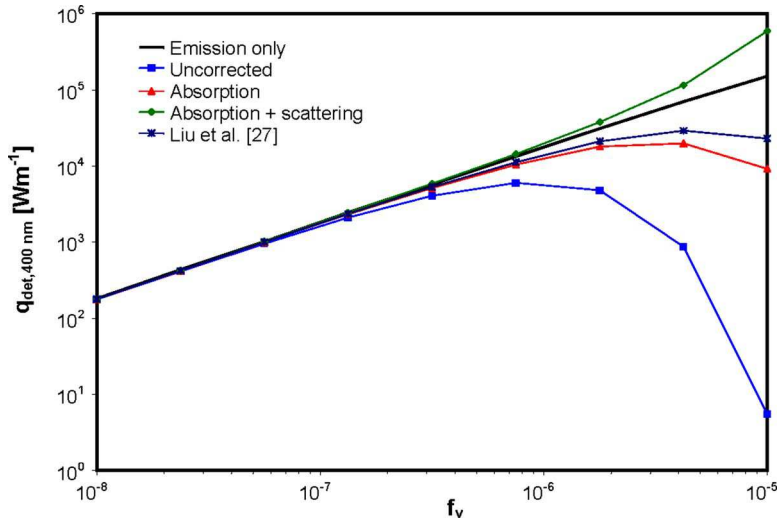

Fig. 8 Comparison of correction schemes for the beam excitation case at λ_d=400 nm

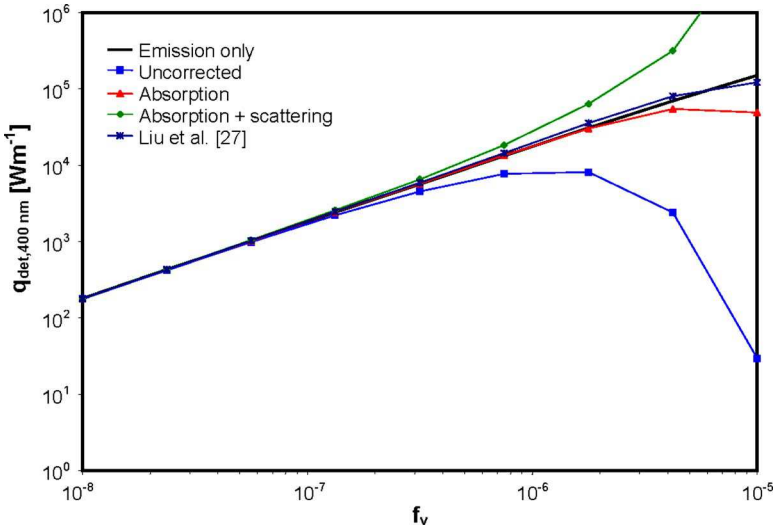

Fig. 9 Comparison of correction schemes for the sheet excitation case at λ_d=400 nm

$$\Phi_p(T_{\text{beam},m},\lambda) = \frac{48\pi^2 c_0^2 h}{\lambda^6}\left[\exp\left(\frac{hc_0}{\lambda k_B T_{\text{beam},m}}\right) - 1\right]^{-1} E(\mathbf{m}_\lambda) \tag{34}$$

The detection wavelength for Eqs. (33) and (34) is chosen to be 780 nm since this channel is least affected by signal trapping.

Figures 10 and 11 show the relative errors in the pyrometric temperatures for beam and sheet excitations, respectively. At higher soot loadings $T_{\text{beam},m}$ underestimates the actual beam temperature because the $q_{\text{det,400 nm}}$ is more strongly attenuated than $q_{\text{det,780 nm}}$, although this effect is somewhat offset by inscatter in the sheet excitation case. The correction schemes generally improve the accuracy of $T_{\text{beam},m}$, although as noted above setting $\kappa_{\lambda,\text{eff}}=\alpha_\lambda+\sigma_{s\lambda}$ overcompensates for outscatter and causes $T_{\text{beam},m}$ to be overestimated, particularly when sheet excitation is used. Figures 12 and 13 and inspection of Eqs. (33) and (34) show that underestimating the pyrometric beam temperature causes f_v to be overestimated except when $\kappa_{\lambda,\text{eff}}=\alpha_\lambda+\sigma_{s\lambda}$ in which case f_v is severely underestimated at high soot loadings, particularly in the case of sheet excitation. The correction proposed by Liu et al. [27] usually gives pyrometric temperatures and soot volume fractions that are closest to the actual values, although again this scheme can only be implemented if the scattering phase function is known.

Conclusions

This paper investigates how scattering influences LII measurements on aerosols containing highly aggregated particles, with a focus on the effect of inscattering when a laser sheet is used to energize the particles instead of a laser beam. The bulk radiative properties of the aerosol are derived from RDG-PFA theory and the radiation analysis is carried out through a BMC simulation. BMC is well suited to modeling LII signals since complex phenomenon such as anisotropic scattering is incorporated into the simulation with ease, and a performance comparison shows BMC to be much more efficient than the traditional FMC implementation for solving this problem.

The analysis shows that signal trapping has a strong effect on LII signals made on aerosols containing highly aggregated soot particles. This effect is most pronounced at short wavelengths due to the spectral dependence of the extinction cross section and increases with soot loading. Inscattering along the optical path

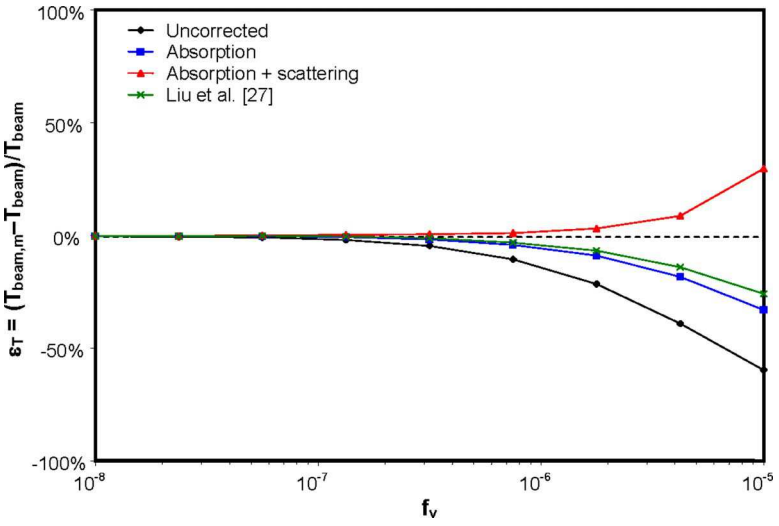

Fig. 10 Relative errors in beam temperature derived using beam excitation

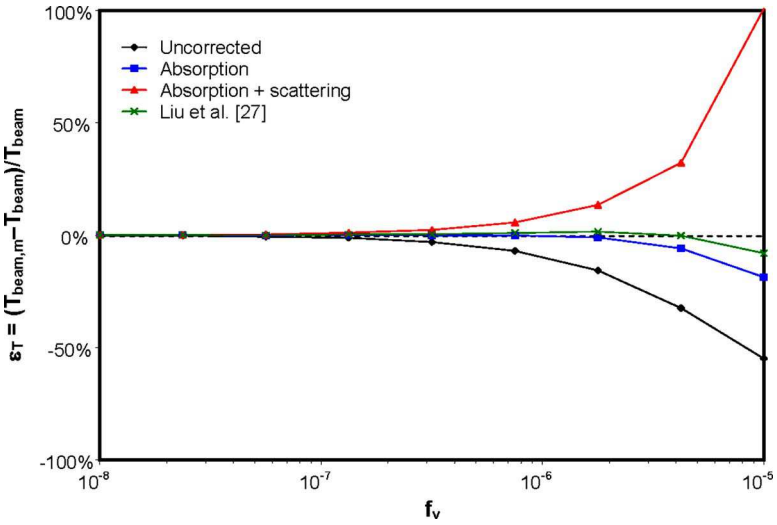

Fig. 11 Relative errors in beam temperature derived using sheet excitation

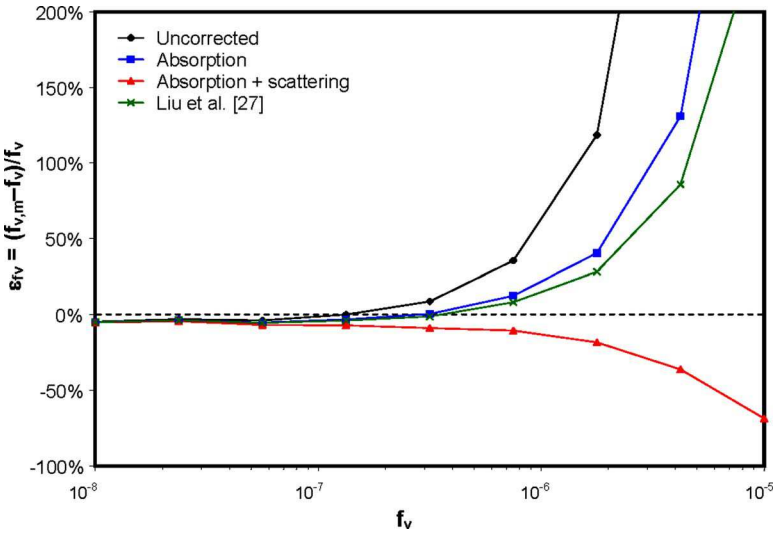

Fig. 12 Relative errors in soot volume fraction derived using beam excitation

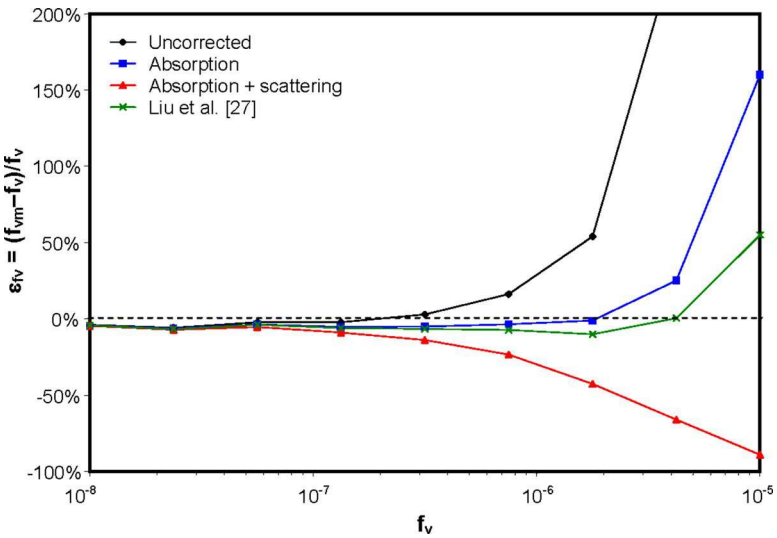

Fig. 13 Relative errors in soot volume fraction derived using sheet excitation

somewhat mitigates signal trapping, however, particularly in the case of sheet excitation. Signal trapping causes the pyrometric temperature derived using LII signals to be underestimated and the soot volume fraction to be overestimated when the latter is calculated using the autocorrelated technique of Snelling et al. [28].

Correction schemes based on Bouguer's law are, on the whole, effective in correcting for signal trapping and extend the range of soot loadings over which accurate LII measurements can be made. The best scheme is the one proposed by Liu et al. [27] that uses the Heyney–Greenstein anisotropy factor, although this parameter is usually available only if independent scattering measurements have been made on the aerosol or if particle morphology distribution parameters are known.

Nomenclature

C_a = absorption cross section, nm^2
C_s = scattering cross section nm^2
D_f = soot aggregate fractal dimension
d_p = primary particle diameter, nm
d_{det} = detector diameter, mm
d_{lens} = lens diameter, mm
$E(\mathbf{m})$ = complex absorption function
$F(\mathbf{m})$ = complex scattering function
f_v = Soot volume fraction
$g_{HG,\lambda}$ = Heyney–Greenstein anisotropy factor
$I_{b,\lambda}$ = blackbody spectral intensity, W m^{-2} nm^{-1} sr^{-1}
I_λ = spectral intensity, W m^{-2} nm^{-1} sr^{-1}
k_g = soot aggregate prefactor
L = aerosol dimension, m
l_s = distance between scattering events, m
$\mathbf{m}$ = complex index of refraction
N_{agg} = aggregate number density, particles m^{-3}
N_p = number of primary particles per aggregate
$N_{p,g}$ = geometric mean number of primary particles per aggregate
$q_{det,\lambda}$ = detector flux, W m^{-1}
R_g = radius of gyration, nm
$\mathbf{r}$ = position vector
T_{beam} = beam temperature, K
T_g = gas temperature, K
w_b = beam width, m
x_p = primary particle size parameter, $\pi d_p/\lambda$
α_λ = absorption coefficient, m^{-1}
ϕ = azimuthal angles, rad
$\kappa_{\lambda,}$ = extinction coefficient, m^{-1}
$\kappa_{\lambda,eff}$ = effective extinction coefficient, m^{-1}
λ = wavelength, nm
η = wave number, nm^{-1}
$\Phi(\theta)$ = phase function
θ = polar angle, rad
θ_{max} = maximum detector acceptance angle, rad
σ_g = geometric standard deviation
$\sigma_{s\lambda}$ = scattering coefficient, m^{-1}

Subscripts and Superscripts

a = absorption
agg = aggregate property
m = measured parameter
n = Monte Carlo trial index
p = primary particle
s = scattering

References

[1] Vander Wal, R. L., and Jensen, K. A., 1998, "Laser-Induced Incandescence: Excitation Intensity," Appl. Opt., **37**, pp. 1607–1616.
[2] Vander Wal, R. L., Zhou, Z., and Choy, M. Y., 1996, "Laser-Induced Incandescence Calibration via Gravimetric Sampling," Combust. Flame, **105**, pp. 462–470.
[3] Snelling, D. R., Smallwood, G. J., Liu, F., Gülder, Ö. L., and Bachalo, W. D., 2005, "A Calibration-Independent Laser-Induced Incandescence Technique for Soot Measurement by Detecting Absolute Light Intensity," Appl. Opt., **44**, pp. 6773–6785.
[4] De luliis, S., Cignoli, F., and Zizak, G., 2005, "Two-Color Laser-Induced Incandescence (2C-LII) Technique for Absolute Soot Volume Fraction Measurements in Flames," Appl. Opt., **44**, pp. 7414–7423.
[5] Roth, P., and Filippov, A. V., 1996, "In Situ Ultrafine Particle Sizing by a Combination of Pulsed Laser Heatup and Particle Thermal Emission," J. Aerosol Sci., **27**, pp. 95–104.
[6] Lehre, T., Jungfleisch, B., Suntz, R., and Bockhorn, H., 2003, "Size Distributions of Nanoscaled Particles and Gas Temperatures From Time-Resolved Laser-Induced-Incandescence Measurements," Appl. Opt., **42**, pp. 2021–2030.
[7] Choy, M. Y., and Jensen, K. A., 1998, "Calibration and Correction of Laser-Induced Incandescence for Soot Volume Fraction Measurements," Combust. Flame, **112**, pp. 485–491.
[8] Köylü, Ü. Ö., and Faeth, G. M., 1994, "Optical Properties of Overfire Soot in Buoyant Turbulent Diffusion Flames at Long Residence Times," ASME J. Heat Transfer, **116**, pp. 152–159.
[9] Liu, F., Thomson, K. A., and Smallwood, G. J., 2007, "Effects of Soot Absorption and Scattering on LII Intensities in Laminar Coflow Diffusion Flames," *Proceedings of the 5th International Symposium on Radiative Transfer*, Bodrum, Turkey, June 17–22.
[10] Chen, L. H., Garo, A., Cen, K., and Grehan, G., 2007, "Numerical Simulation of Soot Optical Diagnostics in Non-Optically Thin Media," Appl. Phys. B: Lasers Opt., **87**, pp. 739–747.
[11] Migliorini, F., De luliis, S., Cignoli, F., and Zizak, G., 2006, "Absorption Correction of Two-Color Laser-Induced Incandescence Signals for Soot Volume Fraction Measurements," Appl. Opt., **45**, pp. 7706–7711.
[12] Shaddix, C. R., and Smyth, K. C., 1996, "Laser-Induced Incandescence Measurements of Soot Production in Steady and Flickering Methane, Propane, and Ethylene Diffusion Flames," Combust. Flame, **107**, pp. 418–452.
[13] McCrain, L. L., and Roberts, W. L., 2005, "Measurement of the Soot Volume Field in Laminar Diffusion Flames at Elevated Pressures," Combust. Flame, **140**, pp. 60–69.
[14] Modest, M. F., 2003, *Radiative Heat Transfer*, 2nd ed., Academic Press, San Diego, CA.
[15] Dobbins, R. A., and Megaridis, C. M., 1991, "Absorption and Scattering of Light by Polydisperse Aggregates," Appl. Opt., **30**, pp. 4747–4754.
[16] Eymet, V., Brasil, A. M., El Hafi, M., Farias, T. L., and Coelho, P. J., 2002, "Numerical Investigation of the Effect of Soot Aggregation on the Radiative Properties in the Infrared Region and Radiative Heat Transfer," J. Quant. Spectrosc. Radiat. Transf., **74**, pp. 697–718.
[17] Murphy, J. J., and Shaddix, C. R., 2005, "Influence of Scattering and Probe-Volume Heterogeneity on Soot Measurements Using Optical Pyrometry," Combust. Flame, **143**, pp. 1–10.
[18] Thomson, K. A., Snelling, D. R., Smallwood, G. J., and Liu, F., 2006, "Laser Induced Incandescence Measurements of Soot Volume Fraction and Effective Particles Size in a Laminar Co-Annular Non-Premixed Methane/Air Flame at Pressures Between 0.5–4.0 MPa," Appl. Phys. B: Lasers Opt., **83**, pp. 469–475.
[19] Modest, M. F., 2003, "Backward Monte Carlo Simulations in Radiative Heat Transfer," ASME J. Heat Transfer, **125**, pp. 57–62.
[20] Siegel, R., and Howell, J. R., 2002, *Thermal Radiation Heat Transfer*, 4th ed., CRC Press, Boca Raton, FL, p. 423.
[21] Yang, B., and Köylü, Ü. Ö., 2005, "Soot Processes in a Strongly Radiating Turbulent Flame From Laser Scattering/Extinction Experiments," J. Quant. Spectrosc. Radiat. Transf., **93**, pp. 289–295.
[22] Chang, H., and Charalampopoulos, T. T., 1990, "Determination of the Wavelength Dependence of Refractive Indices of Flame Soot," Proc. R. Soc. London, Ser. A, **430**, pp. 570–591.
[23] Case, K. M., 1957, "Transfer Problems and the Reciprocity Principle," Rev. Mod. Phys., **29**, pp. 651–663.
[24] Farmer, J. T., and Howell, J. R., 1998, "Comparison of Monte Carlo Strategies for Radiative Transfer in Participating Media," Adv. Heat Transfer, **31**, pp. 333–429.
[25] Toublanc, D., 1996, "Henyey-Greenstein and Mie Phase Functions in Monte Carlo Radiative Transfer Computations," Appl. Opt., **35**, pp. 3270–3274.
[26] Smith, W. J., 1990, *Modern Optical Engineering: The Design of Optical Systems*, 2nd ed., McGraw-Hill, New York, pp. 211–212.
[27] Liu, F., Garbett, E. S., and Swithenbank, J., 1992, "Effects of Anisotropic Scattering on Radiative Heat Transfer Using the P_1-Approximation," Int. J. Heat Mass Transfer, **35**, pp. 2491–2499.
[28] Snelling, D. R., Smallwood, G. J., Liu, F., Gulder, O. L., and Bachalo, W. D., 2005, "A Calibration-Independent Laser-Induced Incandescence Technique for Soot Measurement by Detecting Absolute Light Intensity," Appl. Opt., **44**, pp. 6773–6785.
[29] Levendis, Y. A., Estrada, K. R., and Hottel, H. C., 1992, "Development of Multicolor Pyrometers to Monitor the Transient Response of Burning Carbonaceous Particles," Rev. Sci. Instrum., **63**, pp. 3608–3622.